A&A 439, 351–359 (2005)
DOI: 10.1051/0004-6361:20042560

Astronomy & Astrophysics

Electron density along a coronal loop observed with CDS/SOHO

I. Ugarte-Urra[1,⋆], J. G. Doyle[1], R. W. Walsh[2], and M. S. Madjarska[3,4]

[1] Armagh Observatory, College Hill, Armagh BT61 9DG, N. Ireland
e-mail: iugarte@ssd5.nrl.navy.mil
[2] Centre for Astrophysics, University of Central Lancashire, Preston, PR1 2HE, UK
[3] Max-Planck-Institut für Sonnensystemforschung⋆⋆, Max-Planck-Str. 2, 37191 Katlenburg-Lindau, Germany
[4] Department of Solar Physics, Royal Observatory of Belgium, Av. Circulaire 3, 1180 Bruxelles, Belgium

Received 17 December 2004 / Accepted 21 April 2005

Abstract. The analysis of a coronal loop observed by CDS and EIT on board SOHO is presented. The loop was situated above the North-East limb at a latitude of ∼48°, being clearly visible in the hottest lines of the dataset, Fe XVI 360.76 Å, i.e. greater than 2 000 000 K. The cooler lines in the sample (i.e. O V 629.73 Å and He I 584.35 Å) showed only a brightening at the footpoints location. Based on the Fe XIV 353.84/334.17 line ratio, the electron density along the loop was determined following three different approaches for the background subtraction. No differences, within the error bars, can be found between the three methods. At the apex, the density is 0.9×10^9 cm^{-3}, while at the footpoint it is 50% greater, i.e. 1.4×10^9 cm^{-3}. The inferred filling factor values along the loop, at the formation temperature of the lines, are in the range 0.2–0.9.
One dimensional hydrodynamic modelling of the loop along a given field line, gravity neglected, was performed. A minimum χ^2 analysis results in a best fit case where the total energy input is directed preferentially to the loop footpoint (the heating rate is three times larger at the base than at the apex). An isochoric solution can not be ruled out completely. The exercise illustrates the necessity of accurate spectral diagnostics in order to derive definite conclusions from theoretical models and suggests the need for simultaneous density and temperature diagnostics.

Key words. Sun: corona – plasmas – hydrodynamics

1. Introduction

Coronal loops extend over a vast range of size and brightness, making the solar corona highly structured. The extent of this structuring has been known since the Skylab era, however, the detail contained within recent SOHO (Solar and Heliospheric Observatory) observations with the Extreme ultraviolet Imaging Telescope (EIT) and the Coronal Diagnostic Spectrometer (CDS) and TRACE (Transition Region And Coronal Explorer) has resulted in many investigations regarding whether these structures are dominated by footpoint heating, uniform heating, asymmetric heating, variable heating, exponential decay heating, apex heating, etc (Reale et al. 2000; Priest et al. 2000; Walsh & Galtier 2000, and references therein). The confirmation that the localization of the heating deposition is as controversial as its nature is demonstrated by the fact that an observational case has been made for each of them, including an example where the same dataset has been interpreted in terms of uniform, footpoint and apex heating (Priest et al. 1998; Aschwanden 2001; Reale 2002). Some of the works have determined temperature profiles along the loops using filter ratios of YOHKOH and TRACE data. These temperature profiles are in turn used to deduce the form of heating and thus the most likely heating mechanism. Some authors, (e.g. Martens et al. 2002; Schmelz et al. 2003; Del Zanna & Mason 2003) have questioned the use of filter ratios and have shown that the temperatures obtained do not describe the state of the loops plasma. Instead, broad-band filter ratios provide at best an average temperature and one should use an emission measure type analysis. These works have insisted on the necessity to complement the high resolution images with a spectroscopic analysis that provides the necessary plasma diagnostics.

In this paper we make use of the spectral capabilities of CDS to determine the electron density along an off-limb coronal loop using the line ratio technique, investigating the problems and uncertainties introduced by several background subtraction methods. Filling factors are also inferred. As a final step, a comparison with a hydrodynamic loop model is presented and the limitations of its conclusions discussed under the observational uncertainties.

In Sect. 2 we outline the present observational data, while Sect. 3 discusses the data reduction including the important point of background subtraction, the loop geometry, electron density and filling factor determination. Section 4 discusses the

⋆ Now in: Naval Research Laboratory, Code 7673, Washington, DC 20375, USA.
⋆⋆ Former Max-Planck-Institut für Aeronomie.

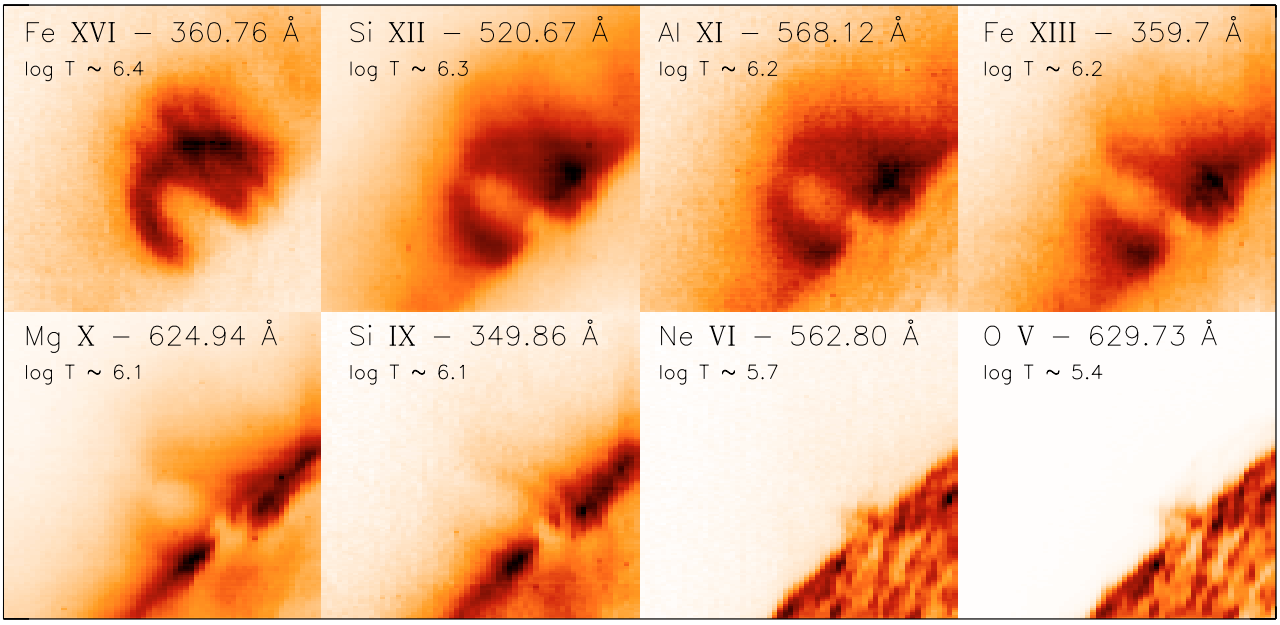

Fig. 1. The coronal loop as observed by CDS on April 1998 at 20:00 in several spectral lines in the temperature range $6.4 \geqslant \log T \geqslant 5.4$ K. The images are in a negative color scale: dark areas represent bright features.

present model calculation while the comparison between the model and the data are outlined in Sect. 5.

2. Observations

The observations were made with the Normal Incidence Spectrometer/CDS (Harrison et al. 1995) on April 6, 1998 starting at 20:00 UT. The rastered image was the result of 60 slit exposures of 90 s each at adjacent solar X positions with the scan mirror moving in the West-East direction. The width of the slit was 4.″064 with a pixel scale of 1.″68 in the North-South direction, so that the final raster has $4' \times 4'$ dimensions with the center located at (–686″, 771″) in heliocentric coordinates.

Standard routines from the CDS software package were applied in order to remove bias, flat-field and cosmic rays, as well as different instrumental effects such as horizontal shifts of the spectrum due to the rotation of the scan mirror and rotation and tilt in the spectrum due to misalignment between grating and detector, and grating and slit. The image was rebinned, summing the intensity of every 3 pixels in the North-South direction to improve the signal-to-noise. The spectral profile for each of these binned pixels was fitted with a Gaussian, removing the continuum emission (mainly due to scattered light from the grating) with a zero order polynomial.

The coronal loop, defined here as a bundle of unresolved strands, was located at a latitude of ~48° above the North-East limb. It was clearly visible in the hottest lines of the dataset, i.e. Fe XVI 360.76 Å ($\log T \sim 6.4$ K), Si XII 520.67 Å and Fe XIV 334.17 Å ($\log T \sim 6.3$ K). For cooler lines ($\log T \leqslant 6.2$ K), like Al XI 568.12 Å, Fe XIII 359.7 Å, Mg X 624.94 Å or Si IX 349.86 Å, the apex becomes fainter, being visible in only the loop legs. The coolest lines of the sample (i.e. Ne VI 562.80 Å, O V 629.73 Å and He I 584.35 Å) showed only a brightening at the footpoints location (see Figs. 1–3).

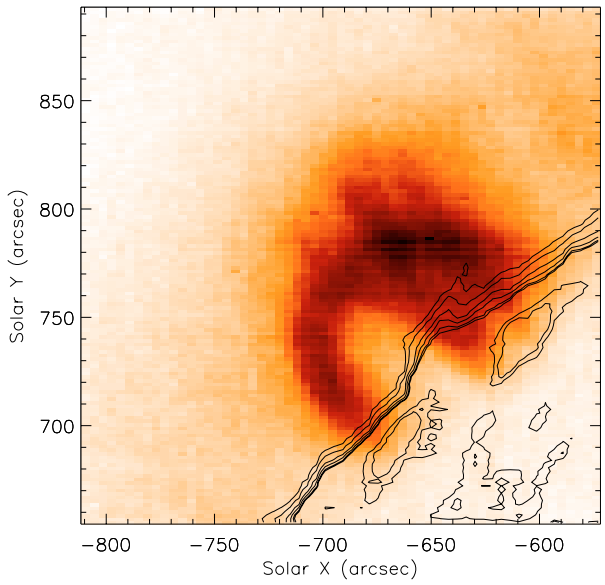

Fig. 2. Loop as seen in Fe XVI 360.76 Å with He I 584.35 Å contours over-plotted.

The loop was also visible in EIT images, taken in the hottest bandpass: Fe XV 284 Å at $\log T \sim 6.3$. The synoptic full disk

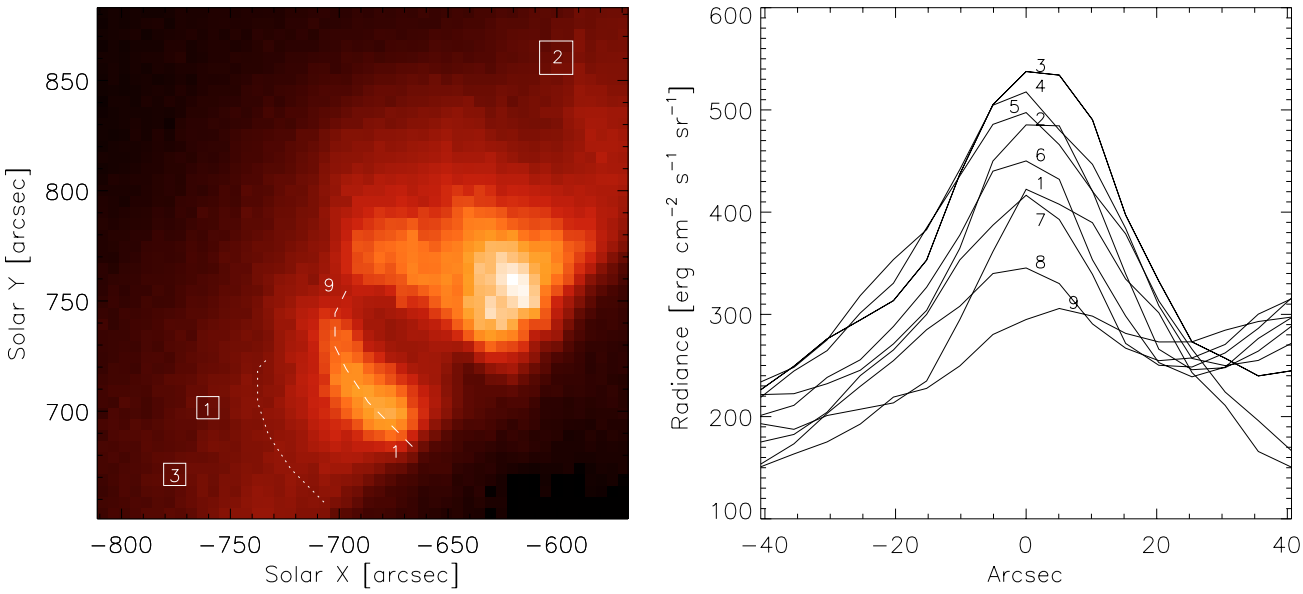

Fig. 3. *Left panel*: loop as seen in Fe XIV 334.17 Å. The square boxes correspond to the three regions used to determine the constant background. The loop's axis and an homologous profile 40″ off-axis are shown with a dashed and a dotted line, respectively. Notice the reverse color scale with respect to Fig. 1. The numbers labeling the loop's axis in the left panel (i.e. 1 and 9) indicate the locations of the first and last perpendicular cross-sections whose radiance is shown in the right panel (see Table 1 and text for details).

images of EIT allowed us to set the lifetime of the loop to be at least 48 h with the loop having a similar shape to that seen with CDS. In EIT, it became diffuse some nine hours after the CDS observations. It was also visible in the SXT/Yohkoh full-field image.

A prominence is visible in He I 584.35 Å situated between the footpoints (see Fig. 2). It is also present in the EIT He II 304 Å images. Full disk Hα images from Big Bear Solar Observatory (BBSO) are not available for this day, however, the previous and following days did show a prominence channel at polar latitudes crossing at the same position. Therefore, in the analysis which follows we only consider the left footpoint and loop leg extending to the apex.

3. Data analysis

3.1. Background subtraction

One of the key steps in the study of a coronal loop is the subtraction of the background (and foreground) emission coming from the plasma which is in the loop's line of sight. Its removal is crucial, for instance, in the case of N_e diagnostics. As shown by Doschek (1984), the line ratio diagnostic from the emission of a region of high density plasma surrounded by a low density plasma would give a misleading electron density value, "a spectroscopic mean density" as defined by Almleaky, Brown, & Sweet (1989). Although it is a well known problem, sometimes the background emission has been neglected or treated improperly and recent works (Reale 2002; Del Zanna & Mason 2003) have outlined the importance of a proper subtraction and the consequences of neglecting it.

In the present work, several approaches of background subtraction have been considered. It is normally assumed that the interpolation of the emission from both sides of a loop is a good representative of its background emission. For that reason, we chose this as our first approach and determined the loop's width and edges using the method developed by Klimchuk (2000). The loop axis, shown as a dashed line over the Fe XIV 334.17 Å image in the left panel of Fig. 3, was visually selected and then straightened using a least square polynomial fit. The pixels corresponding to the loop were visually identified and extracted in order to perform the linear interpolation between background values at the edges of the loop. This analysis was done twice with a second run in which the loop was expanded by one pixel at both sides in order to account for subjective visual bias. We note here that the emission on the left side of the loop axis decays very slowly with no real jump in intensity as expected for a loop feature. This fact, which can be seen at the right panel in Fig. 3, makes it difficult to establish the left edge of the loop. This panel shows cross-sections of the loop perpendicular to the loop's axis. It fits well, however, with the general picture shown by *TRACE* images which show a crowded coronal landscape of loops that can not be resolved by CDS. The edge was finally selected at around −15″ from the loop's axis, where a slight change in the steepness of the curve can be noticed, and which coincides with our visual identification. The right edge was chosen based on the flat region between the loop legs at the right panel in Fig. 3, i.e. around 25″ off-axis. The intensity in this region is higher than the intensity on the left far side of the axis, which could be due to a change in the physical conditions of the surroundings with a brighter background between the legs, or result from the broad point spread function of CDS (Pauluhn et al. 1999) which rises the emission in such

Table 1. Electron density values, in units of 10^8 cm^{-3}, along the nine sections in which we divided the half length of the loop. N_e was determined from the Fe XIV 353.84/334.17 density sensitive line ratio following three different approaches of background subtraction described in the text. Distance along the loop is given in arcseconds from the footpoint.

	1	2	3	4	5	6	7	8	9
Interpolated	$13.7^{+10.8}_{-8.9}$	$7.9^{+3.0}_{-2.8}$	$10.0^{+3.0}_{-2.7}$	$10.8^{+3.4}_{-3.1}$	$10.2^{+3.2}_{-3.1}$	$8.5^{+3.9}_{-3.5}$	$7.2^{+4.6}_{-4.2}$	$8.3^{+9.9}_{-7.3}$	$15.1^{+15.2}_{-12.0}$
Polynomial	$13.6^{+3.8}_{-3.4}$	$10.6^{+1.1}_{-1.0}$	$10.2^{+0.8}_{-1.0}$	$10.1^{+0.8}_{-0.9}$	$10.0^{+0.9}_{-0.9}$	$9.8^{+1.0}_{-1.1}$	$9.0^{+1.4}_{-1.4}$	$8.1^{+2.0}_{-2.1}$	$9.2^{+3.6}_{-3.4}$
Constant 1	$12.9^{+4.2}_{-3.7}$	$9.6^{+2.1}_{-2.0}$	$9.7^{+1.9}_{-1.9}$	$9.6^{+2.0}_{-1.9}$	$9.5^{+2.1}_{-2.0}$	$9.0^{+2.2}_{-2.2}$	$7.9^{+2.6}_{-2.4}$	$9.0^{+3.3}_{-3.2}$	$9.1^{+3.9}_{-3.5}$
Constant 2	$14.3^{+4.4}_{-4.1}$	$10.2^{+2.1}_{-2.1}$	$10.2^{+2.0}_{-2.0}$	$10.1^{+2.1}_{-1.9}$	$10.1^{+2.1}_{-2.1}$	$9.7^{+2.4}_{-2.2}$	$8.7^{+2.5}_{-2.5}$	$10.1^{+3.6}_{-3.4}$	$10.5^{+4.2}_{-3.8}$
Constant 3	$12.3^{+4.0}_{-3.6}$	$9.4^{+2.1}_{-2.0}$	$9.5^{+1.8}_{-1.9}$	$9.4^{+1.9}_{-1.9}$	$9.1^{+2.1}_{-1.9}$	$8.7^{+2.2}_{-2.1}$	$7.6^{+2.4}_{-2.4}$	$8.5^{+3.2}_{-3.0}$	$8.6^{+3.7}_{-3.4}$
No subtraction	$9.0^{+1.8}_{-1.7}$	$8.0^{+1.3}_{-1.3}$	$8.2^{+1.1}_{-1.2}$	$8.0^{+1.2}_{-1.1}$	$7.8^{+1.2}_{-1.1}$	$7.4^{+1.3}_{-1.2}$	$6.6^{+1.2}_{-1.2}$	$6.9^{+1.4}_{-1.3}$	$6.8^{+1.4}_{-1.4}$
Distance	2.5	12.9	23.125	34.2	42.0	51.765	63.735	78.9	93.99

a narrow gap. We consider alternative background subtraction approaches because of the difficulty of an unambiguous identification of the loop edges.

As a second approach, we selected three square regions far apart above the limb, trying to avoid the low-lying loops near the solar surface. The sections selected are shown in Fig. 3 labeled with a number. The averaged emission for each of these three regions was independently subtracted from the emission along the loop (dashed line) for each of the lines before doing the ratio. In a third approach, a radial profile (dotted line in Fig. 3) was selected on the left side, 40″ apart from the loop's axis, fitting it with a polynomial and then subtracting it from the loop's emission. The purpose was to remove a background emission which has the same radial decay of the emission off limb.

3.2. Loop geometry

The loop geometry was obtained assuming that the loop has a semicircular shape contained in a single plane. Based on this assumption an ellipse was fitted to points along the loop deriving an angle of 35° with the line of sight from the ratio of the two semi-axis. With these considerations the semi-length of the loop is 7.2×10^4 km. The footpoints were chosen after a visual inspection and comparison of the loop in different lines, as the co-spatial base of the brightening visible in He I 584 Å and Si X 356 Å lines on the disk.

3.3. Density diagnostics

It is well known that the electron density, N_e, can be determined spectroscopically from the intensity ratio of lines of the same ion (e.g. Mariska 1992). In the present work, we determined N_e along the loop using the electron density sensitive line ratio of Fe XIV 353.84/334.17 and the CHIANTI (Dere et al. 1997; Young et al. 2003) atomic database using Mazzotta et al. (1998) ionization equilibrium. The Fe XIV 353.84 Å line has an unresolved blend (in CDS) with an Al VII line at 353.78 (see for example Brooks et al. 1999; Del Zanna 1999), but it is weak in active region plasma (3% in the active region studied by Thomas & Neupert 1994) and would be even smaller in the off-limb conditions of the present dataset, so it was

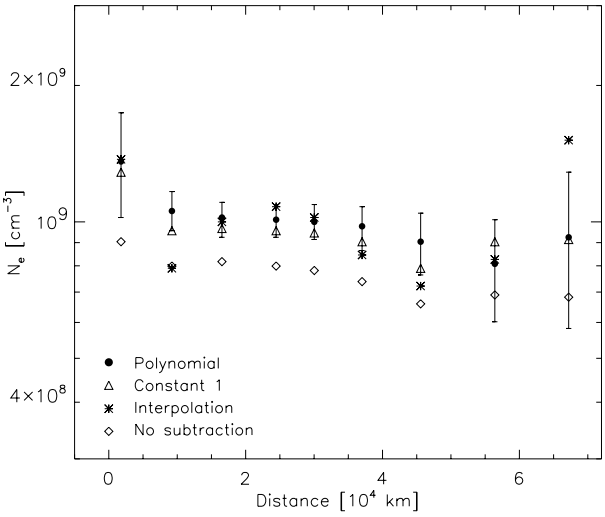

Fig. 4. Electron density along the half length of the loop as obtained from three background subtraction approaches compared to the case with no subtraction. The origin in distance corresponds to the footpoint location. The error bars of the polynomial approach are overplotted.

disregarded. We divided the loop (half-length) in nine sections of ten arc-seconds each and summed the emission in order to improve the signal-to-noise ratio.

The N_e values obtained with the three approaches are shown in Table 1 and are plotted in Fig. 4. The asterisk symbols represent the electron density obtained from the interpolated background (first approach); the triangle symbols represent the density after subtracting constant background 1 (second approach); the filled circles represent the density values obtained after subtracting the polynomial background (third approach); and finally we plot with diamonds, as a comparison, the density values obtained with no background subtraction. For the sake of clarity, only the values for one of the constant background are shown. The results are similar for the other two cases. For the same reason we only plot the error bars corresponding to the polynomial approach. The uncertainties from different approaches overlap. The error bars are large because the steepness of the line ratio vs. electron density curve is not very

pronounced in the range of electron densities found for the loop, which therefore implies that small changes in the ratio lead to large electron density changes. The larger error bars close to the apex are due to the fact that the loop becomes fainter in that part and there is more uncertainty in the background subtraction. This is more noticeable in the case of the interpolated background because the emission of the background is comparable to emission from the loop (see loop's cross-section number 9 in Fig. 3). As expected, in the case of no background being subtracted, the values are systematically lower due to the contribution of material in the line-of-sight at lower N_e.

Finding no difference between the results of the three approaches, and having in the interpolated case a large uncertainty in the final point, we chose the values resulting from the polynomial case as those to be confronted with the fits of a hydrodynamic model (see Sect. 4). The electron density at the loop apex is 0.9×10^9 cm^{-3}, while at the footpoint it is 50% greater, i.e. 1.4×10^9 cm^{-3}.

3.4. Column emission measure and filling factor

The radiance of an optically thin line can be expressed as

$$I(\lambda_{ij}) = \frac{1}{4\pi} \int_d \Delta E_{ij}\, N_j(X^{+n})\, A_{ji}\, \mathrm{d}h \quad [\mathrm{erg\ cm^{-2}\ s^{-1}\ sr^{-1}}] \quad (1)$$

where $\Delta E_{ij} = h\nu_{ij} = hc/\lambda_{ij}$, N_j is the population of the excited level j of the X^{+n} ion (cm^{-3}), A_{ji} is the spontaneous radiative transition probability (s^{-1}), and h measures distance along the line of sight in the volume of emitting plasma, with d the total length. It can be rewritten in terms of the ionization fraction $N(X^{+n})/N(X) = F(T)$, the abundance of the element X relative to hydrogen $Ab(X) = N(X)/N(\mathrm{H})$, and the fraction of abundance of hydrogen relative to the electron density $N(\mathrm{H})/N_e$ (~0.83 for coronal conditions), as

$$I(\lambda_{ij}) = \frac{1}{4\pi} \int_d \Delta E_{ij}\, \frac{N_j(X^{+n})}{N(X^{+n})}\, F(T)\, Ab(X)\, 0.83\, N_e\, A_{ji}\, \mathrm{d}h. \quad (2)$$

This can be re-written as

$$I(\lambda_{ij}) = \frac{\Delta E_{ij}\, Ab(X)}{4\pi} \int_d G(T, N_e)\, N_e^2\, \mathrm{d}h \quad (3)$$

where

$$G(T, N_e) = 0.83\, F(T)\, \frac{N_j(X^{+n})}{N(X^{+n})}\, \frac{A_{ji}}{N_e} \quad (4)$$

is called the *contribution function*.

Equation (3) is normally simplified assuming that the function $G(T, N_e)$, sharply peaked in temperature, at a given electron density can be approximated by a constant value in a narrow temperature region around the peak (Pottasch 1963). In this case we have chosen an interval of 0.3 dex interval around T_{mem}, the temperature of maximum emission where $G(T)$ peaks. With these considerations

$$I = \frac{1}{4\pi}\, \Delta E\, Ab(X)\, C_\lambda\, \mathrm{EM_h} \quad (5)$$

where $C_\lambda = \frac{\int G(T)\mathrm{d}T}{T_{\mathrm{mem}}(10^{0.15} - 10^{-0.15})}$ and $\mathrm{EM_h} = \int_d N_e^2\, \mathrm{d}h$ is the *column emission measure*. Strictly, only a fraction of the volume is emitting the observed radiation. This does not mean that part of the volume is empty, but that there is a distribution of different temperatures and densities inside that volume (see Klimchuk & Cargill 2001, for a more detailed discussion). The *filling factor* f is the parameter used to quantify this fraction and it can be obtained from

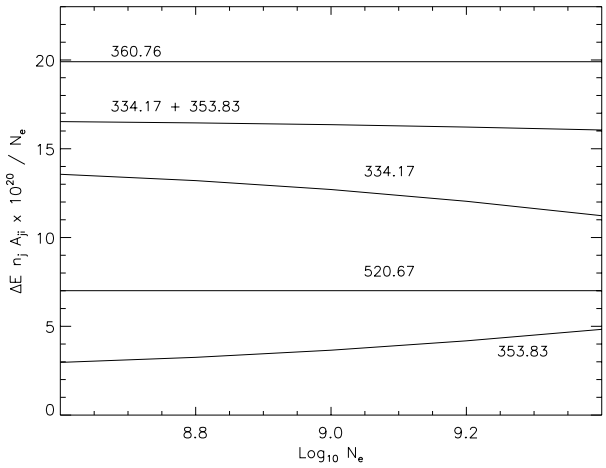

Fig. 5. The electron density sensitivity of various lines in the dataset.

$$f = \frac{\mathrm{EM_h}}{N_e^2\, d} \quad (6)$$

assuming that there is an average electron density in the volume, the density at which C_λ was calculated and, in the case of the present work, different for every loop section.

The emission measure is best constructed with lines which are not sensitive to electron density changes (i.e. $A_{ji}\, N_j(X^{+n}) \propto N_e$). The loop can only be clearly discriminated from the background in certain lines of the dataset: Fe XIV, Fe XVI, Si XII. The Fe XIV lines (334.17 Å and 353.84 Å) do not verify the condition on their own, but the sum of the two gives a fairly constant ratio of $A_{ji}\, N_j(X^{+n})$ versus N_e, in the range of densities found for the loop sections, see Fig. 5. The emission measure was then obtained from the sum of the two observed intensities in each loop section using the iron abundance of Fludra & Schmelz (1999) and Mazzotta et al. (1998) ionization equilibrium. To determine the filling factor we used the loop width (cross-section) d obtained with the method described in the background subtraction section.

The derived values are in the range 0.1–0.7 when considering the intensity in each section as the result of the subtraction of the interpolated background from the edges of the loop, and using the corresponding electron density. Arguing that the electron density has large uncertainties in certain points, we also determine the filling factor using the electron density from the polynomial approach. In this case, they are in the range 0.2–0.5. As previously mentioned, the interpolated background could be over estimated due to the high values of the intensity in the space between the legs as a consequence of the low spatial resolution of CDS. Keeping the width of the loop, but subtracting a less contaminated background intensity from the profile 40″ apart from the loop axis, the filling factor increases to values

ranging from 0.4 to 0.9, which would be upper limits in terms of the uncertainty in the background subtraction.

The Fe XVI and Si XII lines do verify the demanded condition (see Fig. 5), but they are Na- and Li-like ions respectively, two isoelectronic sequences with an anomalous behaviour (Del Zanna et al. 2002), and therefore they are not the most suitable for the emission measure analysis. The loop, however, is better defined in Fe XVI 360.76 Å and the edges easier to determine. The filling factor values obtained from it are lower than the ones presented above, ranging from 0.1 to 0.2. Landi et al. (2002) found for ions of these isoelectronic sequences an emission measure a factor of 2 lower than for other sequences, which could explain why the filling factor values for Fe XVI 360.76 Å are smaller. We also find in our results that the discrepancy is due to smaller emission measure values for Fe XVI and not to a loop's width or density factor.

4. Loop model calculations

Recently several authors have compared an observed thermal structure along a loop with a theoretically derived temperature profile. The main driver for any local variation in the temperature is how the heat deposition in the structure is varying spatially. The results from this approach have been mixed with the cases of uniformly distributed (Priest et al. 2000), apex dominant (Reale 2002) and base dominant (Aschwanden et al. 2001) all being reported. Hydrodynamic modelling of coronal loops has been addressed extensively by several authors (Peres 1999, and references therein). In contrast with the papers mentioned above, this current investigation employs a model for a coronal loop, posed under a number of simplifying assumptions, in order to compare the simulations with the density profile derived in the previous section.

Firstly, it is assumed that the corona is a low β plasma such that any subsequent plasma motions are along the field. The dynamical system reduces to one dimension along a given field-line. Secondly, although it is possible the observed loop consists of a bundle of unresolved strands, for the purposes of this analysis the assumption is made that each strand is acting identically. Thus the governing hydrodynamic equations for a single strand, with gravity neglected, are (Walsh et al. 1996),

$$\frac{D\rho}{Dt} + \rho\frac{\partial v}{\partial s} = 0, \tag{7}$$

$$\rho\frac{Dv}{Dt} = -\frac{\partial p}{\partial s} + \rho\nu\frac{\partial^2 v}{\partial s^2}, \tag{8}$$

$$\frac{\rho^\gamma}{\gamma - 1}\frac{D}{Dt}\left(\frac{p}{\rho^\gamma}\right) = \kappa_0\frac{\partial}{\partial s}\left(T^{5/2}\frac{\partial T}{\partial s}\right) - \rho^2 Q(T) + H(s), \tag{9}$$

$$p = \frac{R}{\tilde{\mu}}\rho T, \tag{10}$$

where s is the distance along the entire length of the field line, v the plasma velocity parallel to the fixed magnetic field, ρ the density, T the temperature, p the gas pressure, γ the ratio of specific heats (equal to 5/3 for a fully ionized plasma like in the solar corona), $\kappa_\parallel = \kappa_0 T^{5/2}$ W m^{-1} K^{-1} the coefficient of thermal conductivity parallel to the field (Braginskii 1965) with $\kappa_0 = 10^{-11}$ for the corona, R the molar gas constant (8.3×10^3 m^2 s^{-2} K^{-1}) and $\tilde{\mu}$ the mean molecular weight with $\tilde{\mu} = 0.6$ mol^{-1} in the ionized corona. The coefficient of kinematic viscosity ν is assumed to be uniform throughout the plasma and Spitzer (1962) gives it as

$$\rho\nu = 2.21\times 10^{-16}\frac{T^{5/2}}{\ln(\Lambda)}\ \mathrm{kg\,m^{-1}s^{-1}}, \tag{11}$$

where $\ln(\Lambda)$ is the Coulomb logarithm which is taken to be approximately 20 for the corona.

The coronal loop (of half-length L_c) is assumed to be symmetrical and thus we can match our theoretical prediction with the section of the loop that is unobscured in the observations. Therefore the boundary conditions are,

$$\frac{\partial\rho}{\partial s} = \frac{\partial p}{\partial s} = 0, \tag{12}$$

at the loop apex ($s = L_c$) and $\rho(0,t) = \rho_c = 1.36\times 10^9$ cm^{-3} and $p(0,t) = p_c$, where p_c is the coronal pressure. Note that ρ_c is the density point at the loop base; the implications for choosing this as a boundary condition are further examined in the next section. As the simulation begins at this first point, the loop half length is $L_c = 7.04\times 10^4$ km.

In the energy Eq. (9), the heat sinks are the strongly temperature-dependent conduction term, plasma radiation $Q(T)$ (Cook et al. 1989) and mass flow to and from the chromosphere. These losses are balanced by a spatially heating term $H(s)$ of the form,

$$H(s) = H_* \exp(\lambda s), \tag{13}$$

where λ and H_* are determined for each specific numerical experiment. The automated procedure for generating the density equilibrium solutions for a range of heating scenarios is as follows. A value for the total energy input for a uniformly distributed heating ($\lambda = 0$) is chosen ($H_{tot} = 2H_0L_c$ for some value of H_0). From an initially isochoric solution (where $\rho = \rho_c$ everywhere), the hydrodynamic code is allowed to relax to the equilibrium corresponding to that particular H_{tot}. Next, the spatial preference in $H(s)$ is examined by increasing(decreasing) incrementally λ away from zero – a corresponding change in H_* allows for the preferred location of the heat deposition to be pushed towards the apex (base) but keeps the total energy content in the loop fixed at H_{tot}. After running through a range of λ values, H_{tot} is altered and the process is repeated.

The numerical scheme employed to evolve this set of coupled, non-linear equations was tested extensively against analytic results obtained using several simplifying assumptions (Walsh et al. 1996).

5. Comparison between model and observations

In order to quantify the comparison between the observed density at the location given and the theoretical predictions, a minimum Chi-squared (χ^2) analysis was employed (as in Priest et al. 2000). That is,

$$\chi^2 = \sum_i \frac{[\rho_{obs}(s_i) - \rho_{mod}(s_i)]^2}{\sigma_i^2}, \tag{14}$$

where $\rho_{obs}(s_i)$ is the observed density at a distance s_i along the strand, $\rho_{mod}(s_i)$ is the model density at the same point and σ_i is

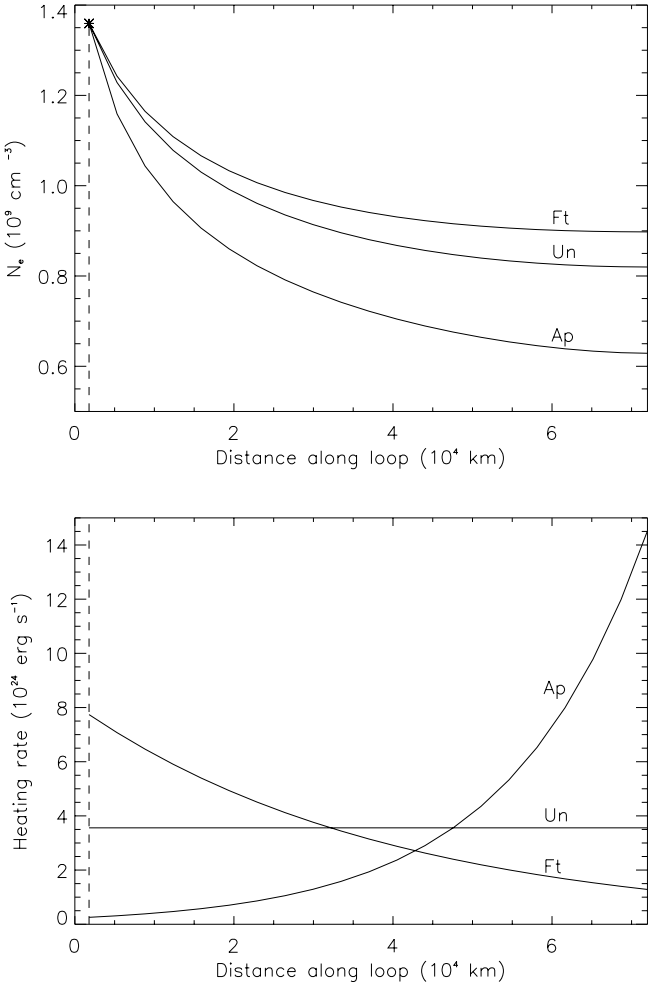

Fig. 6. Typical heating cases for a uniform heating rate of 3.55×10^{24} erg s^{-1} where the top panel is the calculated density profiles corresponding to uniform (Un), apex (Ap) and base/footpoint (Ft) dominant heating as displayed in the bottom panel.

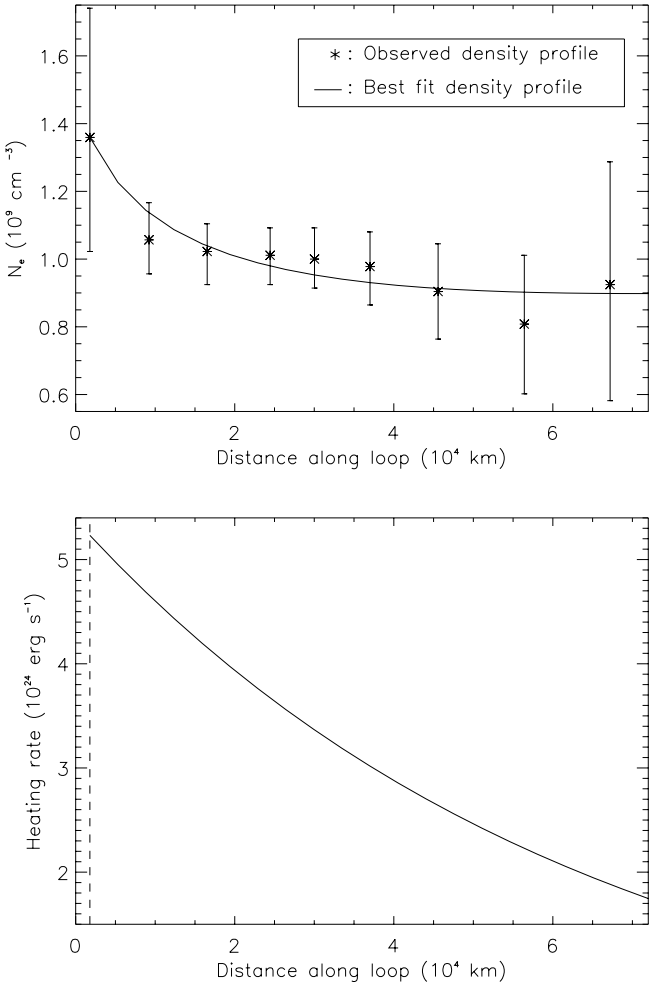

Fig. 7. Case A: (*top panel*) the overall lowest χ^2 fit for the theoretically derived density compared to the observed data; (*bottom panel*) the corresponding $H(s)$.

the standard deviation in the observed density. In the same way as Mackay et al. (2000), the total error bar at a given observed point is treated as $6\sigma_i$.

Figure 6 shows a typical heating case where the value for a uniform heating rate is 3.55×10^{24} erg s^{-1}. In the top panel, the different density profiles are displayed for the corresponding apex dominant (Ap), base or footpoint dominant (Ft) and spatially uniform (Un) experiments displayed in the bottom panel. However, in each case, the total amount of heat that the strand receives is constant; this demonstrates clearly that the location of the heat input can have an important and observable effect on the density structure.

Having generated and compared over thirty thousand individual solutions, the best fit, χ^2 minimum results are displayed in Table 2 for a range of cases. One important aspect to note is that from all the values of $H_{\rm tot}$ considered, the apex dominant heating scenario always had a larger χ^2 value than the corresponding uniform heating case. Thus, apex dominant heating was not considered as a viable heating solution to create the observed density structure.

Table 2. χ^2 minimum values for *case A*: best fit for all solutions; *case B*: best fit for uniform heating only; *case C*: best fit when the boundary condition is set at the maximum density within the observational error bar and *case D*: an isochoric solution.

Case	$\chi^2_{\rm min}$	$H_{\rm tot}$ (10^{24} erg s^{-1})	λ
Case A	13.1	3.17	–2.2
Case B	18.3	2.78	0
Case C	25.3	5.34	–7.7
Case D	16.2	–	–

Each case is described as follows. Case A has the minimum χ^2 found overall and is shown in Fig. 7. The top panel has the density profile relative to the observed density values along with the error bars for each observed point. In the bottom panel, the spatially varying energy input is displayed for this best fit; the best solution appears as a footpoint or base dominant heat deposition. For comparison, case B in Table 2 is the minimum χ^2 value for uniform heating only. The density profile for that case is shown in Fig. 8 (top panel).

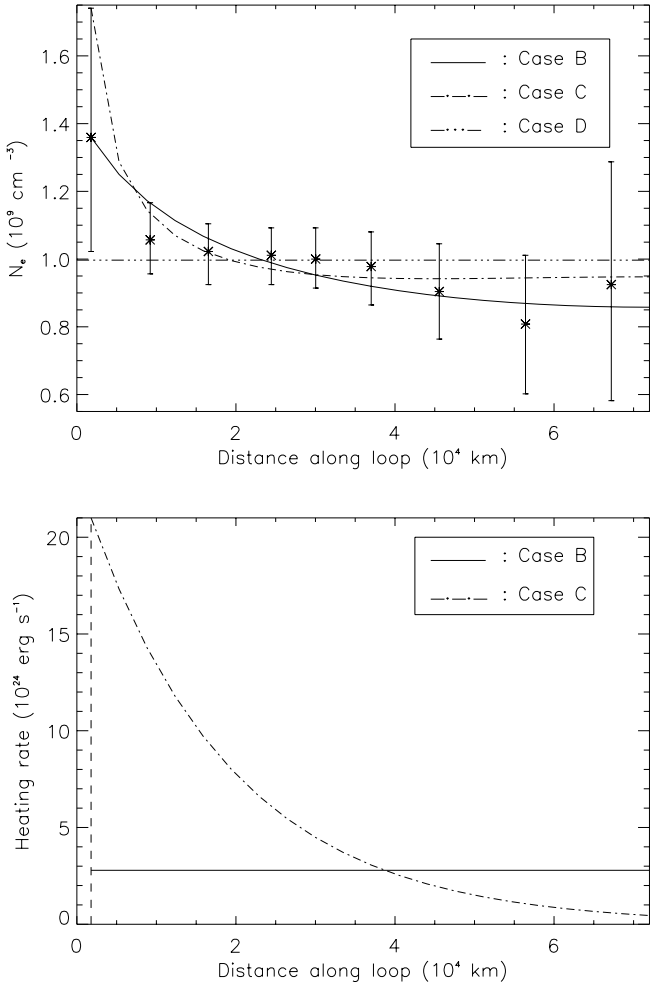

Fig. 8. *Top panel*: best fit comparison for density profiles under cases B, C and D. *Bottom panel*: corresponding heating profiles for cases B and C.

It should be noted that there is a minimum λ value at which a stable, lower apex density solution exists. As outlined in Antiochos et al. (1999), if the energy deposition is too localized at the base, a thermal condensation occurs. These high density apex solutions are not considered in this analysis given the observed density profile under consideration.

One of the assumptions for generating these model comparisons is that the fixed point boundary condition lies on the density point at the loop base. To investigate the impact of this on the analysis, two extreme scenarios are considered. Firstly, the solutions were rerun but with the case of the fixed point tied to the highest value in the error bar for the density point at the loop base. Case C in Table 1 displays the lowest χ^2 values for this case while Fig. 8 once again plots this fit against the observed density profile. The calculated χ^2 is larger than for case A. Even if the first data point is effectively removed from the analysis (using only observational points 2 to 9), the smallest χ^2 value is still larger than that found in case A (15.2 and 13.1 respectively).

Secondly, an isochoric solution (case D) was tested by assuming a constant density exists along the structure and then comparing that with the observed values. The minimum χ^2 for this case is also shown in Fig. 8. Again, this χ^2 value is larger than case A.

Cases C and D highlight the sensitivity of the boundary condition when comparing the observations with the simulations. If footpoint dominant heating is operating in this structure, then, for the numerical model employed, the structure will be dominated by a constant density profile along much of its length (and hence the isochoric case might "fit well" by eye).

6. Summary

As indicated in the introduction, as much as the nature of the heating mechanism of coronal loops, the localization of the heating deposition is still a controversial issue. Here, we have used line ratios to derive the electron density variability along a coronal loop, paying special attention to the background subtraction, the main source of errors, and have used it as an input to modelling. We find, using a one dimensional hydrodynamic model, a minimum χ^2 analysis results in a best fit case where the total energy input is directed preferentially to the loop footpoint. However, due to the large uncertainties in the electron density measurements, an isochoric solution can not be ruled out completely. The current exercise illustrates the necessity of accurate spectral diagnostics in order to derive definite conclusions from theoretical models and suggests the need for simultaneous density and temperature diagnostics.

Regarding future observations, the dynamic nature of the corona must not be ignored. Unfortunately, the present data did not have sufficient spatial and spectral resolution to enable information concerning flows to be derived. In addition to a series of density profile snapshots, temperature information will be required to comprehend fully the evolution of the loop plasma. The present results, limited by the uncertainties in the electron density measurements, show that further electron density diagnostic observations of the type discussed here, but with higher sensitivities, should be undertaken as observable density variations along the loop can be highly dependent on the spatial variation in the heat input. A rastering spectrometer (such as SOHO/CDS and the upcoming SolarB/EIS) also have the problem of requiring some time (often several minutes) to build up the required image area as the slit travels across the target. This could be overcome by setting the slit on one location in the loop (to examine the evolution) but at the expense of observing the entire loop structure. Also there is still controversy over whether the basic loop threads are still to be resolved. Bundles of individual strands averaged out due to pixel resolution could give a very different observational outcome (and hence physical interpretation) to the "loop" than the nature of the constituent strands separately. Therefore, it seems clear that for current and future missions, using a spectrometer and imager simultaneously on the same target is vital.

Acknowledgements. Research at Armagh Observatory is grant-aided by the N. Ireland Dept. of Culture, Arts and Leisure. This work was supported by PPARC grants PPA/G/S/2002/00020 & PPA/V/S/2003/00049 and by a PRTLI research grant for Grid-enabled Computational Physics of Natural Phenomena (Cosmogrid). RWW was funded for this research by a Leverhulme Trust Research Fellowship. We would like to thank the CDS team, in particular

A. Fludra, for his help in these observations. We would also like to thank the anonymous referee for useful comments that helped us to improve the text.

References

Almleaky, Y. M., Brown, J. C., & Sweet, P. A. 1989, A&A, 224, 328
Antiochos, S. K., MacNeice, P. J., Spicer, D. S., & Klimchuk, J. A. 1999, ApJ, 512, 985
Aschwanden, M. J. 2001, ApJ, 559, L171
Aschwanden, M. J., Schrijver, C. J., & Alexander, D. 2001, ApJ, 550, 1036
Braginskii, S. I. 1965, Rev. Plasma Phys., 1, 205 (New York: Leontovich A.V., Consultant Bureau)
Brooks, D. H., Fischbacher, G. A., Fludra, A., et al. 1999, A&A, 347, 277
Cook, J. W., Cheng, C.-C., Jacobs, V. L., & Antiochos, S. K. 1989, ApJ, 338, 1176
Del Zanna, G. 1999, Ph.D. Thesis, University of Central Lancashire, UK
Del Zanna, G., Landini, M., & Mason, H. E. 2002, A&A, 385, 968
Del Zanna, G. & Mason, H. E. 2003, A&A, 406, 1089
Dere, K. P., Landi, E., Mason, H. E., Monsignori Fossi, B. C., & Young, P. R. 1997, A&AS, 125, 149
Doschek, G. A. 1984, ApJ, 279, 446
Fludra, A., & Schmelz, J. T. 1999, A&A, 348, 286
Harrison, R. A., Sawyer, E. C., Carter, M. K., et al. 1995, Sol. Phys., 162, 233
Klimchuk, J. A. 2000, Sol. Phys., 193, 53
Klimchuk, J. A., & Cargill, P. J. 2001, ApJ, 553, 440
Landi, E., Feldman, U., & Dere, K. P. 2002, ApJS, 139, 281
Mackay, D. H., Galsgaard, K., Priest, E. R., & Foley, C. R. 2000, Sol. Phys., 193, 93
Mariska, J. T. 1992, The solar transition region, Cambridge Astrophysics Series (New York: Cambridge University Press)
Martens, P. C. H., Cirtain, J. W., & Schmelz, J. T. 2002, ApJ, 577, L115
Mazzotta, P., Mazzitelli, G., Colafrancesco, S., & Vittorio, N. 1998, A&AS, 133, 403
Pauluhn, A., Rüdi, I., Solanki, S. K., et al. 1999, Appl. Opt., 38, 7035
Peres, G. 1999, in ESA SP-446: 8th SOHO Workshop: Plasma Dynamics and Diagnostics in the Solar Transition Region and Corona, 43
Pottasch, S. R. 1963, ApJ, 137, 945
Priest, E. R., Foley, C. R., Heyvaerts, J., et al. 1998, Nature, 393, 545
Priest, E. R., Foley, C. R., Heyvaerts, J., et al. 2000, ApJ, 539, 1002
Reale, F. 2002, ApJ, 580, 566
Reale, F., Peres, G., Serio, S., et al. 2000, ApJ, 535, 423
Schmelz, J. T., Beene, J. E., Nasraoui, K., et al. 2003, ApJ, 599, 604
Spitzer, L. 1962, Physics of Fully Ionized Gases (Physics of Fully Ionized Gases, New York: Interscience (2nd edition), 1962)
Thomas, R. J., & Neupert, W. M. 1994, ApJS, 91, 461
Walsh, R. W., Bell, G. E., & Hood, A. W. 1996, Sol. Phys., 169, 33
Walsh, R. W., & Galtier, S. 2000, Sol. Phys., 197, 57
Young, P. R., Del Zanna, G., Landi, E., et al. 2003, ApJS, 144, 135